# 9
# Narrow-Linewidth Lasers on a Silicon Chip

**Edward H. Bernhardi and Markus Pollnau**

**Abstract** Diode-pumped distributed-feedback (DFB) channel waveguide lasers were demonstrated in $Er^{3+}$-doped and $Yb^{3+}$-doped $Al_2O_3$ on standard thermally oxidized silicon substrates. Uniform surface-relief Bragg gratings were patterned by laser-interference lithography and etched into the $SiO_2$ top cladding. The maximum grating reflectivity exceeded 99 %. Monolithic DFB cavities with Q-factors of up to $1.35 \times 10^6$ were realized. The $Er^{3+}$-doped DFB laser delivered 3 mW of output power with a slope efficiency of 41 % versus absorbed pump power. Single-longitudinal-mode operation at a wavelength of 1545.2 nm was achieved with an emission line width of $1.70 \pm 0.58$ kHz, corresponding to a laser Q-factor of $1.14 \times 10^{11}$. Yb3+-doped DFB lasers were demonstrated at wavelengths near 1,020 nm with output powers of 55 mW and a slope efficiency of 67 % versus launched pump power. An $Yb^{3+}$-doped dual-wavelength laser was achieved based on the optical resonances induced by two local phase shifts in the DFB structure. A stable microwave signal at ~15 GHz with a –3-dB width of 9 kHz and a long-term frequency stability of ±2.5 MHz was created via the heterodyne photo-detection of the two laser wavelengths. Interaction of the intra-cavity evanescent laser field with micro-particles in contact with the grating surface induces changes in the microwave beat signal, whose detection enabled real-time detection and accurate size measurement

E.H. Bernhardi (✉) • M. Pollnau
Integrated Optical Microsystems Group, MESA+ Institute for Nanotechnology, University of Twente, P.O. Box 217, 7500 AE Enschede, The Netherlands
e-mail: M.Pollnau@utwente.nl

B. Di Bartolo et al. (eds.), *Nano-Structures for Optics and Photonics*,
NATO Science for Peace and Security Series B: Physics and Biophysics,
DOI 10.1007/978-94-017-9133-5_9, © Springer Science+Business Media Dordrecht 2015

of single micro-particles with diameters ranging between 1 and 20 μm, which represents the typical size of many fungal and bacterial pathogens. A limit of detection of ~500 nm was deduced.

## 9.1 Introduction

Monolithic lasers find numerous applications in spectroscopy, optical communications, and optical sensing. These applications often place stringent requirements with respect to efficiency, output power, spectral characteristics, compactness, robustness, and thermal stability on the laser. Waveguide lasers are of particular importance for the realization of compact, rigid, and robust optical devices, since the entire laser cavity along with the optical feedback elements can be fabricated on the same substrate. Besides, when an application requires a laser array, e.g. for simultaneous operation over a specific wavelength range, cost issues strongly favor an on-chip integrated approach. In this work, surface-corrugated Bragg gratings are integrated with $Al_2O_3$ channel waveguides to realize a variety of monolithic distributed-feedback (DFB) and distributed-Bragg-reflector (DBR) cavities in rare-earth-ion-doped $Al_2O_3$ waveguides.

## 9.2 Waveguide Fabrication, Spectroscopy, and Gain

The $Al_2O_3$ ridge channel waveguides were fabricated in 1-μm-thick $Al_2O_3$ layers which were deposited onto standard thermally oxidized silicon wafers [1]. For the $Er^{3+}$-based laser device a doping concentration of $3 \times 10^{20}$ cm$^{-3}$ was used, while the $Yb^{3+}$-based laser devices had a doping concentration of $5.8 \times 10^{20}$ cm$^{-3}$. All the waveguides supported single-transverse-mode operation at the respective pump and laser wavelengths and were 10 mm long, 2.5–3.0 μm wide, and etched to a depth of ~0.1 μm via a chlorine-based reactive ion etching process [2]. For $Er^{3+}$ concentrations in the range of $1–2 \times 10^{20}$ cm$^{-3}$, internal net gain was obtained over a wavelength range of 80 nm (1,500–1,580 nm) and a peak gain of 2.0 dB/cm was measured at 1,533 nm [3]. The influence of energy migration and energy-transfer upconversion among neighboring $Er^{3+}$ ions on luminescence decay and steady-state population densities in $Al_2O_3 : Er^{3+}$ thin films was investigated by means of photoluminescence decay measurements under quasi-CW excitation. A fast quenching process induced by, e.g., active ion pairs and clusters, undesired impurities, or host material defects such as voids, that was not revealed by any particular signature in the luminescence decay curves because of negligible emission by the quenched ions under quasi-CW excitation, was verified by pump-absorption experiments [4]. This quenching process strongly affects device performance of $Al_2O_3 : Er^{3+}$ as an amplifier, to a lesser extent also of $Al_2O_3 : Yb^{3+}$, but it affects a lasing device only by increasing its threshold [5]. The first laser in an $Al_2O_3$ layer on a silicon chip was demonstrated utilizing a micro-ring cavity [6].

## 9.3 High-$Q$ Passive Cavities

For the fabrication of Bragg gratings [7], a plasma-enhanced chemical vapor deposition (PECVD) $SiO_2$ cladding layer was deposited on top of the ridge waveguides. The uniform surface-relief Bragg gratings were fabricated on the top surface of the PECVD $SiO_2$ cladding by means of laser interference lithography (LIL). A grating pattern was defined in a 120-nm-thick negative resist layer on top of the PECVD cladding and was etched into the $SiO_2$ layer using a $CHF_3$ : $O_2$ reactive ion plasma. The grating period varied between 316 nm for the $Yb^{3+}$-doped devices, with a Bragg wavelength of ~1,020 nm, to 507 nm for the passive cavities with a Bragg wavelength of ~1,590 nm. Transverse and axial cross-sectional views of the waveguide laser structure are displayed in Fig. 9.1.

Cavities with exceptionally high $Q$-factors are required for the realization of narrow-linewidth lasers and highly sensitive integrated optical sensors. Fifteen different DBR cavities were fabricated in order to investigate their grating reflectivity, finesse, and $Q$-factor. The length of the Bragg gratings on either side of the DBR cavities was varied from 1.25 to 4.75 mm in steps of 0.25 mm, with the distance between the Bragg reflectors chosen such that the total physical cavity length was 10 mm in all cases, with a grating coupling coefficient of $\kappa = 6.5\,\mathrm{cm}^{-1}$. The reflectivity of the Bragg reflectors could be inferred from the measured finesse of each respective cavity [7]. The Bragg gratings deliver reflectivities higher than 99 % for TE polarization, as shown in Fig. 9.2, due partly to the waveguide propagation losses (including grating-induced scattering losses) being as low as 0.14 dB/cm. Measured $Q$-factors exceed $1.02 \times 10^6$ (TE polarization) for these DBR cavities. In addition to the DBR cavities, numerous DFB cavities were also fabricated and characterized.

In order to induce quarter-wavelength phase-shifts in the 10-mm-long uniform Bragg gratings, as is required for the DFB cavities, a 1-mm-long localized adiabatic sinusoidal tapering of the waveguide width was fabricated in the center region of

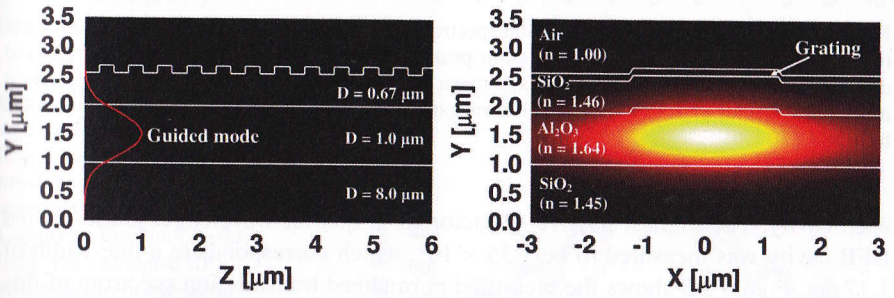


**Fig. 9.1** (*Left*) A transverse cross-sectional view of the waveguide layer structure showing the calculated TE mode profile. (*Right*) An axial cross-sectional view of the waveguide structure showing the thickness $D$ of each layer (Figure taken from Ref. [7])

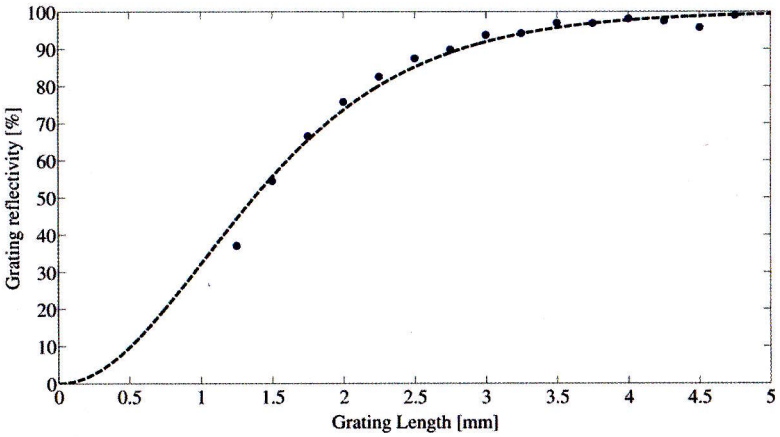


**Fig. 9.2** Grating reflectivity at the Bragg wavelength for TE polarization as a function of grating length. The *blue dots* represent the reflectivity as determined from the measured finesse, while the *dashed line* is the predicted reflectivity according to coupled mode theory (Figure taken from Ref. [7])

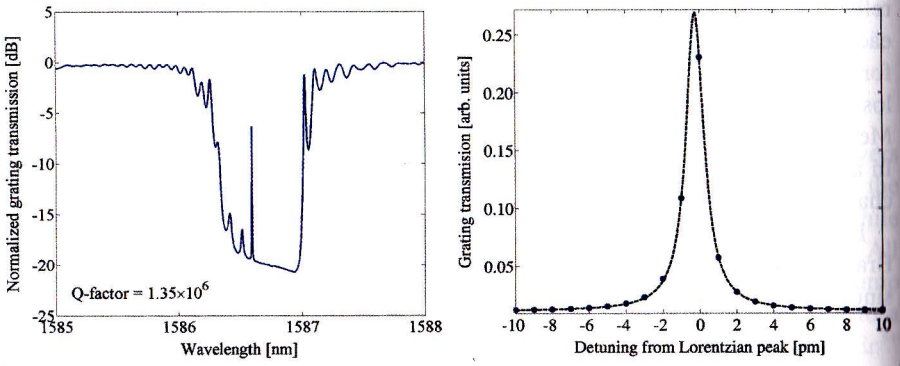


**Fig. 9.3** (*Left*) Measured TE transmission spectrum for the passive DFB cavity. (*Right*) Enlargement of the single Fabry-Pérot transmission peak in (a), where the *blue dots* are the measured data points, while the *dashed line* is a Lorentzian fit to the data. This peak represents the highest measured $Q$-factor of $1.35 \times 10^6$, which corresponds to a linewidth of 1.17 pm (Figure modified from Ref. [7])

each cavity. The highest passive $Q$-factor for a quarter-wavelength phase-shifted DFB cavity was measured to be $1.35 \times 10^6$, which corresponds to a line-width of 1.17 pm. Figure 9.3 shows the measured normalized transmission spectrum of this particular cavity where the high-quality resonance is clearly visible.

## 9.4 Narrow-Linewidth Waveguide Lasers

Making use of the Bragg grating-based cavity configurations and distributed quarter-wavelength phase shifts which were described in the previous section, DFB cavities were realized in $Er^{3+}$-doped as well as $Yb^{3+}$-doped $Al_2O_3$ waveguides. The 1,480-nm-diode-pumped $Al_2O_3 : Er^{3+}$ DFB laser exhibits a threshold of 2.2 mW absorbed pump power and a maximum laser output power of more than 3 mW at the maximum available pump power of 67 mW, resulting in a slope efficiency of 41 % versus absorbed pump power [8], see Fig. 9.4. The laser operates TE-polarized at a wavelength of 1,545.2 nm with an emission linewidth of 1.7 kHz, as inferred from a self-heterodyne coherence measurement whose result is shown in Fig. 9.5. This value corresponds to a laser $Q$-factor [9] of $1.14 \times 10^{11}$.

Recently, these results have been picked up by research groups at the Massachusetts Institute of Technology and the University of California in Santa Barbara. Both groups exploited a low-loss $SiN/SiO_2$ waveguide structure [10], where the SiN core included a side-relief grating, and deposited an $Al_2O_3 : Er^{3+}$ layer on top, thereby demonstrating a laser [11] as well as a laser array [12]. An $Al_2O_3 : Yb^{3+}$ DFB laser [13], which was diode-pumped at 976 nm, exhibited a threshold of

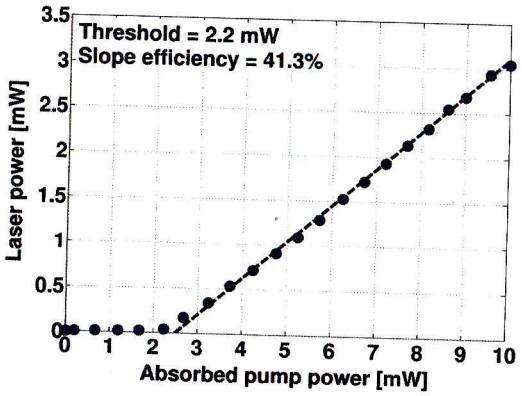


**Fig. 9.4** Laser output power of the DFB laser as a function of absorbed pump power (*circles*). The *dashed line* represents a linear fit with a slope efficiency of 41.3 % (Figure taken from Ref. [8])

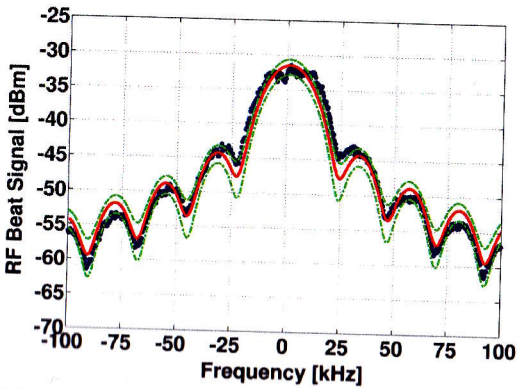


**Fig. 9.5** Measured RF beat signal (*circles*) of the DFB laser, along with the best fitted theoretical RF power spectrum of a 1.70 kHz Lorentzian linewidth (*solid line*). The calculated RF power spectrum curves for Lorentzian linewidths of $1.70 + 0.58$ kHz (*dashed line*) and $1.70 - 0.58$ kHz (*dash-dotted line*) enclose 68 % of the measured data (Figure taken from Ref. [8])

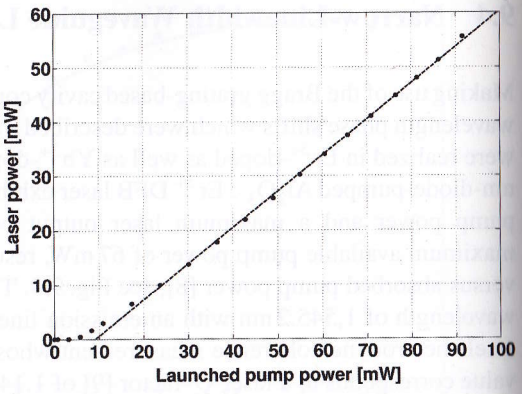


**Fig. 9.6** Measured input-output power characteristics of the $Al_2O_3 : Yb^{3+}$ DFB channel waveguide laser (Figure modified from Ref. [13])

5 mW, see Fig. 9.6. The laser operated at a wavelength of 1,022.2 nm where the maximum measured laser output power exceeded 55 mW at a launched pump power of 91.5 mW, resulting in a slope efficiency of 67 %. The differences in the performance of the two lasers are explained largely by the higher absorption cross-section and the absence of energy-transfer upconversion in the $Yb^{3+}$ compared to the $Er^{3+}$ system. A monolithic distributed-Bragg-reflector channel waveguide laser in $Yb^{3+}$-doped aluminum oxide was also demonstrated [14]. Single-longitudinal-mode and single-polarization operation was achieved at a wavelength of 1,021.2 nm. Continuous-wave output powers of up to 47 mW and a launched pump power threshold of 10 mW resulted in a slope efficiency of 67 %. The high output power and high efficiency of the $Al_2O_3 : Yb^{3+}$ waveguide lasers along with the absorption coefficient of water, which is about 50 times smaller at a wavelength of ~1,020 nm as compared to $Er^{3+}$ emission wavelengths around 1,550 nm [15], make such monolithic $Al_2O_3 : Yb^{3+}$ waveguide lasers ideal for bio-sensing applications.

## 9.5 Dual-Wavelength Waveguide Lasers

Aside from these monolithic single-longitudinal-mode $Al_2O_3$ waveguide lasers, monolithic dual-wavelength, or dual-longitudinal-mode, $Al_2O_3$ waveguide lasers were also realized. The main purpose for using dual-wavelength lasers, in this work, is to create a stable electrical beat signal at the output of a photodetector, with the frequency of the beat signal corresponding to the wavelength spacing of the two optical waves. The operation of the dual-wavelength cavity is based on two localized quarter-wavelength phase shifts in a DFB cavity [16], see Fig. 9.7. When two phase shifts are induced in a uniform waveguide Bragg grating, two resonance peaks appear in the transmission stop-band of the device. The two resonances share a common cavity which consists of both phase-shift regions, and the wavelength spacing between these resonances and longitudinal field distributions depend on the spatial separation and values of the respective phase shifts.

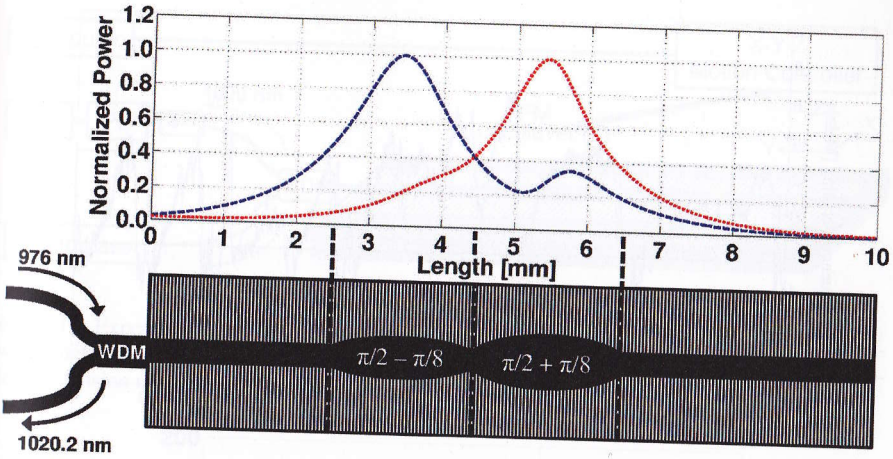


**Fig. 9.7** Schematic of the dual-wavelength DFB cavity, along with the calculated longitudinal field distribution of the two respective laser wavelengths (Figure modified from Ref. [17])

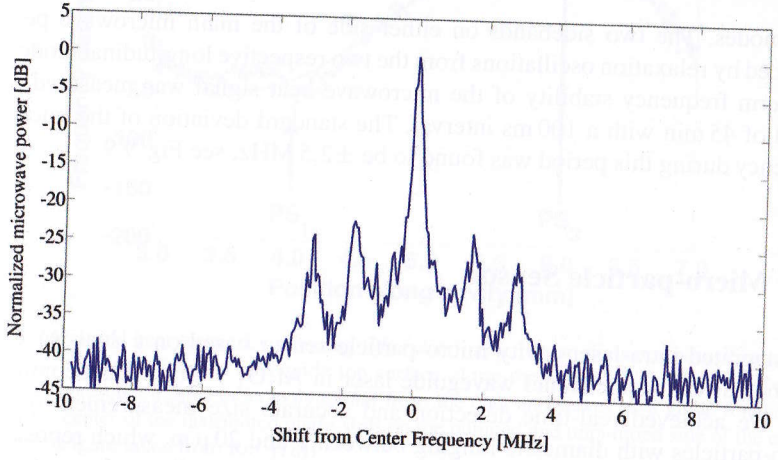


**Fig. 9.8** Electrical spectrum of the microwave beat signal centered at 15.0426 GHz (Figure modified from Ref. [17])

A 10-mm-long $Yb^{3+}$-doped DFB cavity with two 2-mm-long distributed phase shifts were fabricated, with the phase shifts centered at 3.5 and 5.5 mm (as measured from the end-facet from where the light is launched) [17]. To confirm that the laser was indeed operating on two longitudinal modes, the laser output was measured with a photodetector and an electrical spectrum analyzer, which confirmed a microwave beat signal at 15.0426 GHz, which is shown in Fig. 9.8. The beat signal frequency implies a wavelength separation of 52 pm between the two individual longitudinal

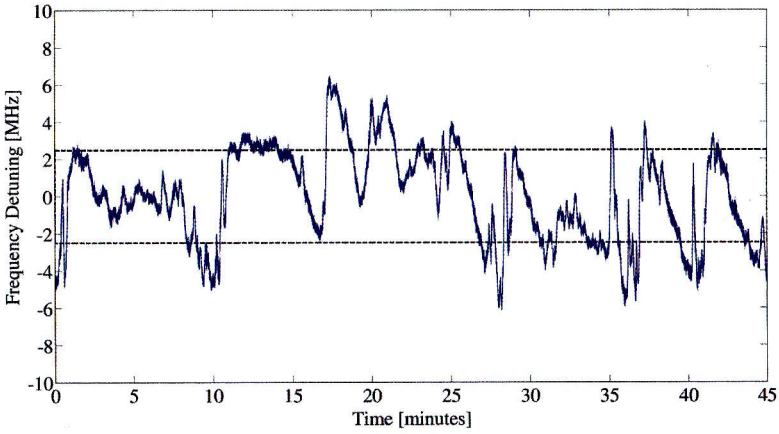


**Fig. 9.9** Measured frequency stability of the microwave signal during a period of 45 min. The standard deviation of the center frequency during this period was ±2.5 MHz, indicated by the *black horizontal dashed lines* (Figure modified from Ref. [17])

laser modes. The two sidebands on either side of the main microwave peak are produced by relaxation oscillations from the two respective longitudinal modes. The long-term frequency stability of the microwave beat signal was measured over a period of 45 min with a 100 ms interval. The standard deviation of the microwave frequency during this period was found to be ±2.5 MHz; see Fig. 9.9.

## 9.6 Micro-particle Sensor

An integrated intra-laser-cavity micro-particle sensor based on a dual-wavelength distributed-feedback channel waveguide laser in $Al_2O_3 : Yb^{3+}$ was demonstrated [18]. We achieved real-time detection and accurate size measurement of single micro-particles with diameters ranging between 1 and 20 μm, which represent the typical sizes of many fungal and bacterial pathogens as well as a large variety of human cells. The sensing principle relies on measuring changes in the frequency difference between the two longitudinal laser modes as the evanescent field of the dual-wavelength laser interacts with micro-sized particles on the surface of the waveguide.

We demonstrated optical sensing by systematically probing the intra-cavity evanescent laser fields with various borosilicate glass microspheres of diameters ranging between 1 and 20 μm. Each microsphere was attached to an atomic force microscope (AFM) cantilever of low stiffness (spring constant 0.01–0.02 N/m). The cantilever was mounted on a 3-dimensional computer-controlled translation stage, as shown in Fig. 9.10. This experimental setup allowed us to scan a microsphere in

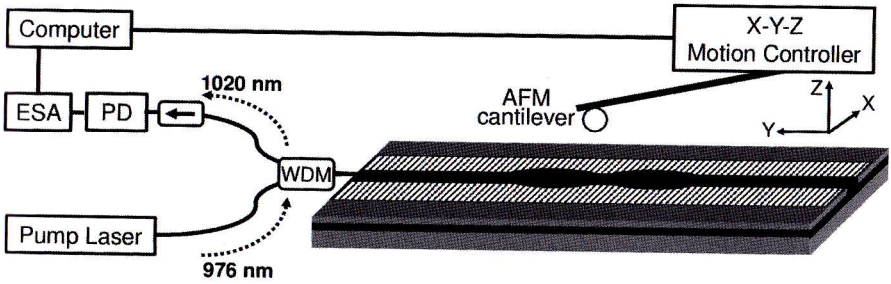


**Fig. 9.10** Experimental setup used to characterize the intra-laser-cavity micro-particle dual-wavelength laser sensor. *ESA*: Electronic spectrum analyzer; *PD*: Photodetector; *WDM*: Wavelength division multiplexing fiber; *AFM*: Atomic force microscope (Figure taken from Ref. [18])

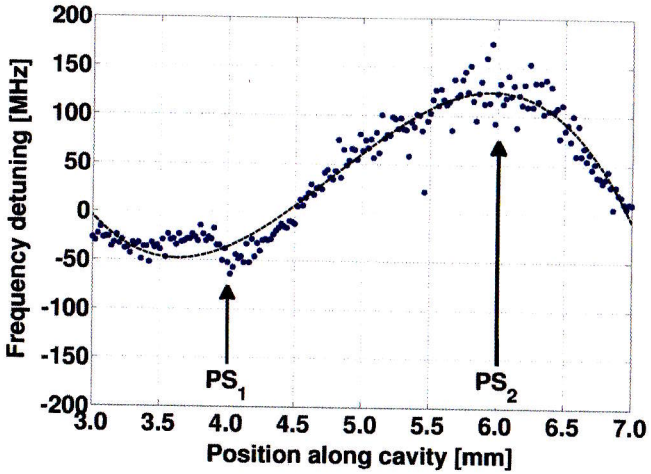


**Fig. 9.11** Measured beat frequency detuning (*blue dots*), as a 10-μm-diameter borosilicate glass microsphere is scanned on the waveguide top surface along the length of the laser cavity. The *dashed line* represents a third-order polynomial fit to the data and serves as a guide for the eye. $PS_1$ and $PS_2$: center of the distributed phase shift on the pumped and unpumped side of the cavity, respectively (Figure taken from Ref. [18])

contact mode across the top surface of the waveguide laser with a lateral resolution of 25 nm, while recording the center frequency of the microwave beat signal for each position of the microsphere.

To illustrate the impact of the particle-induced scattering loss on the microwave beat frequency, we scanned a 10-μm-diameter borosilicate glass microsphere on the waveguide top surface along a 4-mm-long section of the laser cavity, covering both distributed phase-shift regions, see Fig. 9.11. Inside the phase-shift region located on the pumped side of the cavity, a negative detuning of the beat signal was observed, while probing the other phase-shift region resulted in a positive detuning [18].

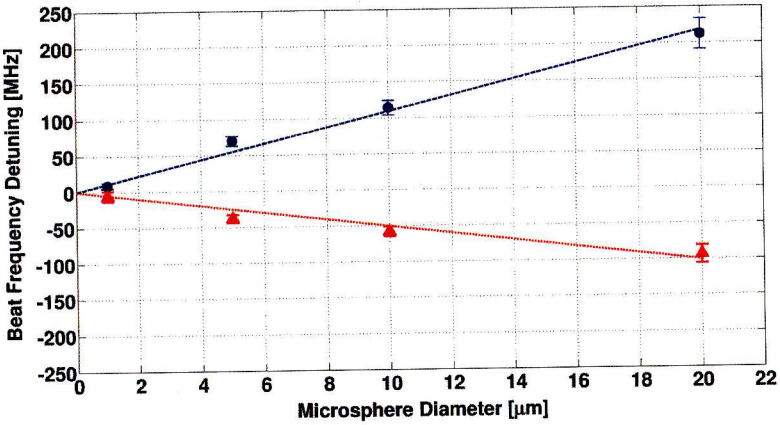


**Fig. 9.12** Laser microwave-beat-frequency detuning as a function of microsphere diameter. The *red triangles* were measured in the center of the phase shift on the pumped side, while the *blue circles* were measured in the center of the phase shift on the unpumped side of the laser cavity. The *red* and *blue lines* represents linear fits through the origin with slopes of −5 and 11 MHz/μm, respectively (Figure taken from Ref. [18])

The interaction between the intra-laser-cavity light fields and the microspheres was further analyzed by performing a 2-dimensional scan on the waveguide surface inside the center of each of the two respective phase-shift regions, using a 5-μm-diameter borosilicate glass microsphere. By averaging along the y-direction (along the length of the waveguide), a single curve could be constructed for the two 2-dimensional surface scan, representing the beat frequency detuning as the microsphere is scanned perpendicular across the waveguide [18].

In order to investigate the size-measurement capability of our dual-wavelength laser sensor, the effect of various sizes of microspheres on the microwave beat frequency was measured. Each microsphere, attached to an AFM cantilever, was scanned across the waveguide laser in the center region of each of the two respective phase shifts, while the frequency detuning of the microwave beat signal was observed, see Fig. 9.12. Inside the first phase-shift region, the largest investigated microsphere with a diameter of 20 μm induced a 94 MHz decrease in the microwave beat signal, while the smallest microsphere, with a diameter of 1 μm, induced a frequency decrease of 6 MHz. In the second phase-shift region, the largest and smallest microspheres induced an increase in the microwave beat signal of 212 and 9 MHz, respectively. Assuming that the frequency detuning of the laser-generated beat signal has a linear dependence on microsphere size, the resolution of the sensor is currently limited to particles of ~500 nm diameter. This size limitation is due to the free-running frequency stability of the laser of ~5 MHz, which is most likely due to fluctuations in the pump power as well as some optical back-reflections into the laser cavity [17].

## 9.7 Summary

Over the past few years we have demonstrated DFB and DBR channel waveguide lasers in rare-earth-ion-doped $Al_2O_3$ on silicon substrates. In an $Er^{3+}$-doped DFB laser, single-longitudinal-mode operation was achieved with an emission line width of 1.7 kHz. $Yb^{3+}$-doped DFB and DBR lasers were demonstrated with output powers of 55 mW and a slope efficiency of 67 %. An $Yb^{3+}$-doped dual-phase-shift DFB laser with dual-wavelength emission was operated and a stable microwave beat signal at ~15 GHz was created via heterodyne photo-detection. By measuring changes in the microwave signal, we could detect single micro-particles with diameters between 1 and 20 μm on the waveguide surface.

## References


1. Worhoff K, Bradley JDB, Ay F, Geskus D, Blauwendraat TP, Pollnau M (2009) Reliable low-cost fabrication of low-loss $Al_2O_3$ : $Er^{3+}$ waveguides with 5.4-dB optical gain. IEEE J Quantum Electron 45:454–461
2. Bradley J, Ay F, Wörhoff K, Pollnau M (2007) Fabrication of low-loss channel waveguides in $Al_2O_3$ and $Y_2O_3$ layers by inductively coupled plasma reactive ion etching. Appl Phys B 89:311–318
3. Bradley JD, Agazzi L, Geskus D, Ay F, Wörhoff K, Pollnau M (2010) Gain bandwidth of 80 nm and 2 dB/cm peak gain in $Al_2O_3$ : $Er^{3+}$ optical amplifiers on silicon. J Opt Soc Am B 27:187
4. Agazzi L, Wörhoff K, Pollnau M (2013) Energy-transfer-upconversion models, their applicability and breakdown in the presence of spectroscopically distinct ion classes: a case study in amorphous $Al_2O_3$ : $Er^{3+}$. J Phys Chem C 117:6759–6776
5. Agazzi L, Bernhardi EH, Wörhoff K, Pollnau M (2012) Impact of luminescence quenching on relaxation-oscillation frequency in solid-state lasers. Appl Phys Lett 100:011109
6. Bradley JD, Stoffer R, Agazzi L, Ay F, Wörhoff K, Pollnau M (2010) Integrated $Al_2O_3$ : $Er^{3+}$ ring lasers on silicon with wide wavelength selectivity. Opt Lett 35:73–75
7. Bernhardi E, Lu Q, van Wolferen H, Wörhoff K, de Ridder R, Pollnau M (2011) Monolithic distributed Bragg reflector cavities in $Al_2O_3$ with quality factors exceeding 106. Photonics Nanostruct Fundam Appl 9:225–234
8. Bernhardi EH, van Wolferen HAGM, Agazzi L, Khan MRH, Roeloffzen CGH, Wörhoff K, Pollnau M, de Ridder RM (2010) Ultra-narrow-linewidth, single-frequency distributed feedback waveguide laser in $Al_2O_3$ : $Er^{3+}$ on silicon. Opt Lett 35:2394–2396
9. Eichhorn M, Pollnau M (submitted 2014) The theory of continuous-wave lasers in the spot light of the vacuum photon
10. Bauters JF, Heck MJR, John DD, Barton JS, Bruinink CM, Leinse A, Heideman RG, Blumenthal DJ, Bowers JE (2011) Planar waveguides with less than 0.1 dB/m propagation loss fabricated with wafer bonding. Opt Express 19:24090–24101
11. Purnawirman, Sun J, Adam TN, Leake G, Coolbaugh D, Bradley JDB, Hosseini ES, Watts MR (2013) C- and l-band erbium-doped waveguide lasers with wafer-scale silicon nitride cavities. Opt Lett 38:1760–1762
12. Belt M, Huffman T, Davenport ML, Li W, Barton JS, Blumenthal DJ (2013) Arrayed narrow linewidth erbium-doped waveguide-distributed feedback lasers on an ultra-low-loss silicon-nitride platform. Opt Lett 38:4825–4828

13. Bernhardi E, van Wolferen H, Wörhoff K, de Ridder R, Pollnau M (2011) Distributed feedback channel waveguide lasers in Erbium- and Ytterbium-Doped $Al_2O_3$ on silicon – OSA technical digest (CD). In CLEO/Europe and EQEC 2011 conference digest, p. CJ10_4, Optical Society of America, Munich
14. Bernhardi EH, van Wolferen HAGM, Wörhoff K, de Ridder RM, Pollnau M (2011) Highly efficient, low-threshold monolithic distributed-Bragg-reflector channel waveguide laser in $Al_2O_3 : Yb^{3+}$. Opt Lett 36:603–605
15. Hale GM, Querry MR (1973) Optical constants of water in the 200-nm to 200-microm wavelength region. Appl Opt 12:555–563
16. Villanueva GE, Perez-Millan P, Palaci J, Cruz JL, Andres MV, Marti J (2010) Dual-wavelength DFB Erbium-Doped fiber laser with tunable wavelength spacing. IEEE Photonics Technol Lett 22:254–256
17. Bernhardi EH, Khan MRH, Roeloffzen CGH, van Wolferen HAGM, Wörhoff K, de Ridder RM, Pollnau M (2012) Photonic generation of stable microwave signals from a dual-wavelength $Al_2O_3 : Yb^{3+}$ distributed-feedback waveguide laser. Opt Lett 37:181–183
18. Bernhardi EH, van der Werf KO, Hollink AJF, Wörhoff K, de Ridder RM, Subramaniam V, Pollnau M (2013) Intra-laser-cavity microparticle sensing with a dual-wavelength distributed-feedback laser. Laser Photonics Rev 7:589–598